ORIGINAL PAPER

Composite Sr- and V-doped LaCrO₃/YSZ sensor electrode operating at low oxygen levels

Anders Lund · Torben Jacobsen · Karin Vels Hansen · Mogens Mogensen

Abstract A porous composite electrode of $La_{0.8}Sr_{0.2}Cr_{0.97}V_{0.03}O_{3-\delta}$ (LSCV) and yttria-stabilised zirconia (YSZ) was evaluated as a possible candidate for high-temperature potentiometric oxygen sensor measuring electrodes. The oxygen processes at the electrode were characterised by performing electrochemical impedance spectroscopy (EIS) measurements between 600 °C and 900 °C at oxygen partial pressures between 4.2×10^{-6} and 0.2 bar. The microstructure of the electrode was characterised by electron microscopy. The LSCV/YSZ electrode was porous and coherent with LSCV and YSZ grain sizes between 200 and 400 nm. At oxygen partial pressures around 0.2 bar at 700 °C, the oxygen reaction is dominated by solid-state diffusion of oxide ions and surface reaction kinetics. At oxygen partial pressures around 10^{-5} bar above 800 °C, gas phase mass transport processes dominate the impedance spectra. The relatively low response time at 700 °C at an oxygen partial pressure of around 5×10^{-6} bar and an inlet gas flow rate of 8 L h^{-1} makes the LSCV/YSZ electrode suitable for use as an potentiometric oxygen sensor electrodes.

A. Lund (✉) · T. Jacobsen
Department of Chemistry, Technical University of
Denmark, 2800 Kgs. Lyngby, Denmark
e-mail: andlund@gmail.com

K. V. Hansen · M. Mogensen
Fuel Cells and Solid State Chemistry Division, Risø National
Laboratory for Sustainable Energy, Technical University of
Denmark, 4000 Roskilde, Denmark

Introduction

Perovskite-type metal oxides are promising candidates for high-temperature potentiometric oxygen gas sensor electrodes and could thus replace platinum which is more expensive and less abundant [1–3]. The oxygen reaction at the platinum electrode is confined to the region near the triple phase boundary, which makes this type of electrode sensitive to impurities segregating from the ceramic electrolyte. However, at the perovskite-type metal oxide electrode, the oxygen reaction may take place at the surface/gas interface because these materials may be mixed ionic and electronic conductive [4–6]. An electrode of a metal oxide may therefore have a higher active area compared with a platinum electrode and may therefore be more resistant towards poisoning by impurities. The metal oxide electrode must be chemically stable in contact with the electrolyte, the thermal expansion must match that of the yttria-stabilised zirconia (YSZ) electrolyte and the volume should not expand significantly by uptake/release of oxygen [7].

The potentiometric oxygen sensor is used because of its stability [8], for example in the food industry where oxygen is detrimental. The potentiometric oxygen sensor consists of two electrodes separated by an oxide ion conducting electrolyte, typically YSZ. The cell develops an electromotive force given by the difference in oxygen partial pressure between the electrodes. Only a very small current is running through the cell which should therefore be characterised at open circuit voltage. The response time, the time it takes to perform a measurement and the accuracy depend on the electrode oxygen processes. The response time should not be more than a few seconds, similar to that of a platinum

electrode. The electrode oxygen processes for metal oxide electrodes are not well described at low oxygen partial pressures around 10^{-6} bar, at which potentiometric oxygen sensors typically operate.

The perovskite-type strontium and vanadium-substituted lanthanum chromite with the formula $La_{0.8}Sr_{0.2}Cr_{0.97}V_{0.03}O_{3-\delta}$ (LSCV), where δ is the deviation from stoichiometry, is a *p*-type conductor and catalytically active towards oxygen [1, 2]. The strontium substitution induces formation of oxide ion vacancies and electron holes, which increases the *p*-type conductivity, around 30 S cm^{-1} at 700 °C at an oxygen partial pressure of 1 bar [9]. The strontium-substituted lanthanum chromite is not reduced significantly down to 10^{-16} bar at 1,000 °C and has nearly the same thermal expansion coefficient as YSZ [10]. Chromium oxide is substituted with vanadium oxide to improve the sinterability which is also improved by mixing LSCV with YSZ to produce a composite electrode [11, 12].

The electrode oxygen processes can be characterised by electrochemical impedance spectroscopy (EIS) in a broad frequency range and thereby separate the oxygen processes by their characteristic frequency. The impedance spectra obtained from measurements on mixed ionic and electronic oxides can be modelled using a Gerischer-type impedance at high oxygen partial pressures [4, 13]. Using this model, the oxygen reaction is related to surface kinetics and solid-state diffusion of oxide ions [4]. Measurements performed on platinum/YSZ cells have shown that gas phase mass transport processes dominate the impedance spectrum at low oxygen partial pressures around 10^{-6} bar. The impedance of these processes is inversely proportional to the oxygen partial pressure [14]. The electrochemical properties are dependent on the microstructure of the electrode, which can be characterised by electron microscopy.

The present paper seeks to evaluate the LSCV/YSZ composite electrode as a candidate for oxygen sensor electrodes. The oxygen processes at the electrode were characterised by performing EIS measurements between 600 °C and 900 °C at oxygen partial pressures between 4.2×10^{-6} and 0.2 bar. The microstructure of the electrode was characterised by electron microscopy.

Experimental

The LSCV powder was synthesized by pyrolysis of an aqueous solution of metal nitrates (>99% purity, Johnson Matthey) with glycine [15]. The powder was calcined at 800 °C for 2 h, and the perovskite phase
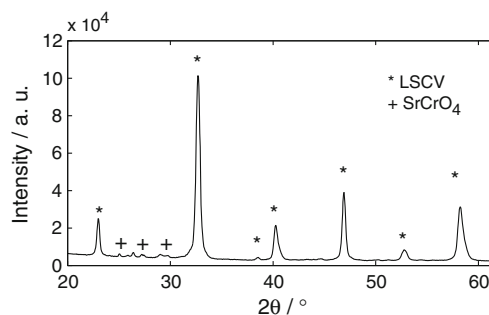

Fig. 1 XRD pattern of the powder after calcination at 800 °C. The *lines* of LSCV [24] and SrCrO$_4$ [25] are marked with *symbols*

was verified by X-ray powder diffraction performed on a Theta–Theta STOE diffractometer. Figure 1 shows the XRD pattern of the calcined powder. A paste of LSCV mixed with 8 mol% YSZ (99.85%, Tosoh Corp.) with a volume ratio between LSCV and YSZ of 1:1 was brush painted on a three-electrode pellet, Fig. 2, YSZ to produce a porous working electrode with an area of 0.39 cm^2. The three-electrode pellet was painted two times and then sintered at 1,200 °C in air for 2 h. The counter and reference electrodes were painted once on the three-electrode pellet using a platinum paste (Engelhard, No: 6082A) and then sintered at 1,000 °C for 2 h.

Figure 2 shows a cross section of the three-electrode pellet of YSZ and the three-electrode setup. The working electrode was placed in a controlled atmosphere of mixed dry N$_2$ and dry air. The oxygen partial pressure could be controlled between 0.2 bar and around 10^{-6} bar, with an accuracy of ±10%, by mixing these gasses or supplying oxygen into flowing N$_2$ by an Pt/YSZ/Pt cell. The oxygen partial pressure at the counter and reference electrode was 0.2 bar. The inlet gas flow rate was between 8 and 15 L h^{-1}. The oxygen partial pressure at the working electrode was monitored by measuring the potential difference be-
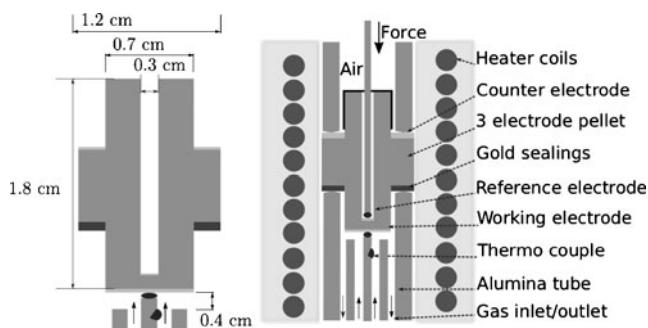

Fig. 2 The cross section of the three-electrode pellet and the test setup

tween the working and the reference electrode and the temperature, which was controlled with an accuracy of ±1 °C. Furthermore, two potentiometric oxygen sensors were used to measure the oxygen partial pressure of the gas inlet and outlet.

Results

Electrode microstructure

Scanning electron microscope (SEM) images of the electrode were obtained using a field emission SEM (Zeiss SUPRA-35). Figures 3 and 4 show SEM images of parts of the electrode along the fractured cross section. Figure 3 shows that the electrode is around 15 μm thick and porous with sub-micrometer-sized particles. The dense YSZ electrolyte is seen in the bottom part of the image. Figure 4 shows that the grains, between 200 and 400 nm in sizes, are networked. The electrode is porous with a pore size of a couple of hundred nanometers.

EIS measurements

EIS measurements were performed with a Solartron 1250 frequency response analyser and a Solartron 1287 potentiostat in a frequency range from 2×10^{-3} Hz to 10 kHz with three to 20 measurements per frequency decade at open circuit voltage with an AC root mean square amplitude of 10 mV. The measurements were performed between 600 °C and 900 °C and between an oxygen partial pressure of 4.2×10^{-6} and 0.2 bar. The EIS data were fitted with equivalent circuit models using the Levenberg–Marquardt algorithm in Matlab.
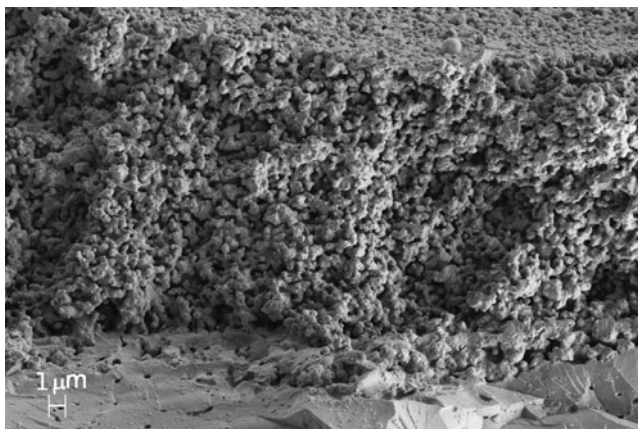

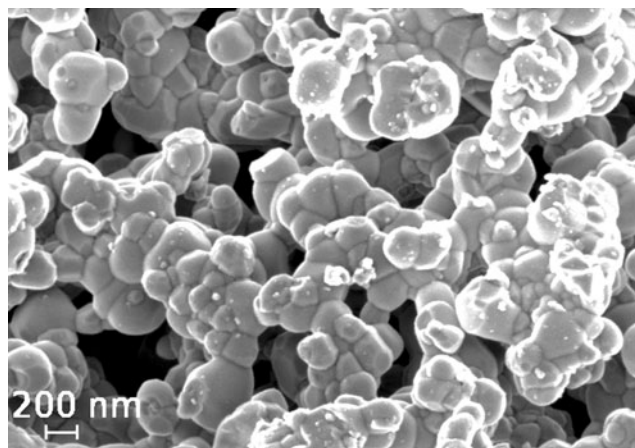**Fig. 3** An SEM image of the porous LSCV/YSZ working electrode

Fig. 4 An SEM image of the porous LSCV/YSZ working electrode

The impedance is normalised with respect to the area of the electrode projection on the electrolyte.

Figure 5 shows that the impedance, Z, increases when the oxygen partial pressure is decreased from 0.21 to 0.062 bar at 700 °C. The impedance spectra consist of at least one depressed arc. The intersection between the impedance at around 2 kHz and the real-axis corresponds to the ohmic loss due to transport of oxide ions through the YSZ electrolyte, around 10 Ω cm². The distance between the working and reference electrode is 0.2 cm, and a rough estimate of the conductivity of the YSZ is then $\sigma = 0.2/10$ S cm$^{-1} = 0.02$ S cm^{-1}, which is in accordance with the bulk oxide ion conductivity of YSZ at 700 °C [16]. The intersection between the impedance at low frequency and the x-axis of the Nyquist plot is equal to the direct current resistance. The polarisation resistance related to the arc was found to be highly temperature dependent which also indicates that the arc represents oxygen reaction kinetics at the electrode.

Figure 6 shows that the impedance increases and the characteristic frequency decreases with decreasing
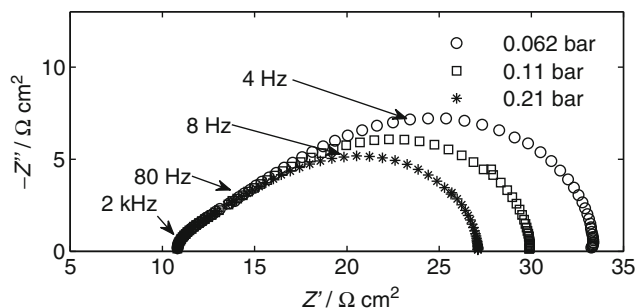

Fig. 5 Nyquist plot for measurements performed at 700 °C and at an inlet flow rate of 8 L h^{-1} at various oxygen partial pressures
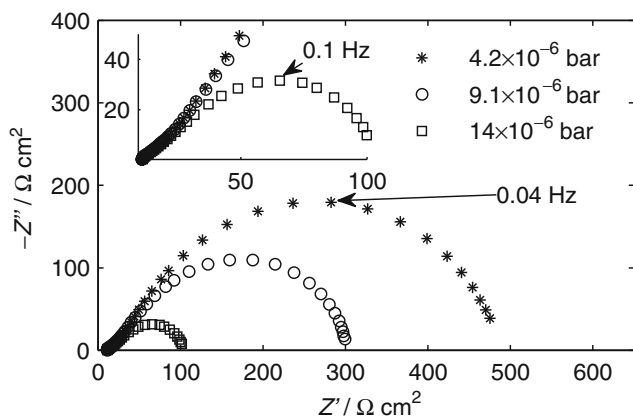
Fig. 6 Nyquist plot for measurements performed at 700 °C and at an inlet gas flow rate of 8 L h^{-1} at various oxygen partial pressures

Fig. 8 Arrhenius plot of the polarisation resistance for measurements performed at an oxygen partial pressure of 10^{-5} bar and at an inlet gas flow rate of 8 L h^{-1}

oxygen partial pressure between 4.2×10^{-6} and 14×10^{-6} bar at 700 °C and at an inlet gas flow rate of 8 L h^{-1}. The measured impedance is much more dependent on the oxygen partial pressure compared with the measurements performed between 0.062 and 0.2 bar. One depressed and nearly symmetrical arc dominates the impedance at 4.2×10^{-6} bar with a characteristic frequency of around 0.04 Hz.

Figure 7 shows that the polarisation resistance, R_p, is proportional to $p_{O_2}^{-0.25}$, between oxygen partial pressures, p_{O_2}, of 0.2 and around 10^{-5} bar. Below 10^{-5} bar, the slope increases which indicates that gas mass transport processes are dominating.

The impedance was measured at various temperatures at an oxygen partial pressure of 10^{-5} bar and at an inlet gas flow rate of 8 L h^{-1}. Figure 8 shows an Arrhenius plot of the polarisation resistance. The slope increases with decreasing temperature, T, probably be-

cause the oxygen reaction dominates the polarisation resistance at low temperatures and the gas phase mass transport processes dominate the polarisation resistance at high temperatures. The resistance related to gas phase mass transport processes is nearly temperature independent while the reaction kinetics are high temperature dependent. For example, the slope of the graph at 650 °C corresponds to an activation energy of 1 eV.

Gas phase mass transport by convection is inversely proportional to the inlet gas flow rate [14, 17]. Figure 9 indicates that the polarisation resistance is inversely proportional to the inlet gas flow rate for measurements performed at an oxygen partial pressure of around 3×10^{-5} bar, at 800 °C. The polarisation resistance was multiplied with the oxygen mole fraction $x_{O_2} = p_{O_2}/P$, where P is the atmospheric pressure, to account for variations in the oxygen partial pressure. The polarisa-
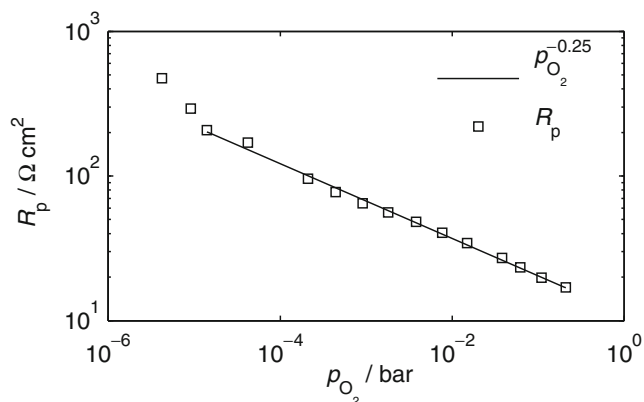

Fig. 7 The polarisation resistance, R_p, as a function of the oxygen partial pressure, p_{O_2}, for measurements performed at 700 °C and at an inlet gas flow rate of 8 L h^{-1}
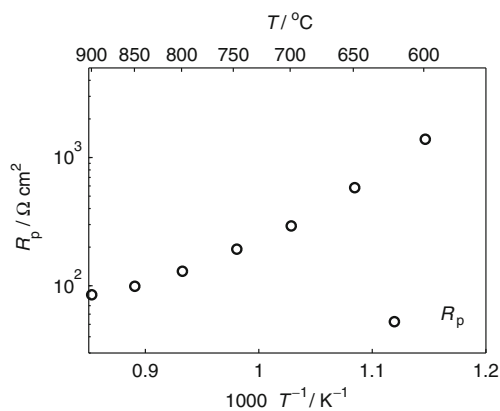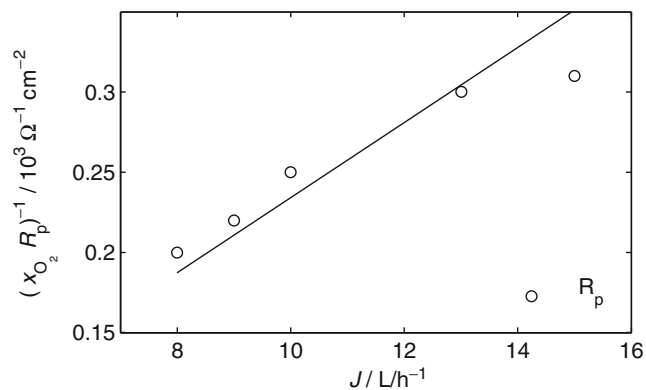

Fig. 9 The inverse of the normalised polarisation resistance, $(R_p x_{O_2})^{-1}$, as a function of the inlet gas flow rate for measurements performed at an oxygen partial pressures of 3×10^{-5} bar at 800 °C. The *solid line* is a linear fit going through the origo

tion resistance is assumed to be dominated by gas phase mass transport processes, for which the impedance is inversely proportional to the oxygen partial pressure. For example, the gas conversion resistance is given by [17]

$$R_C = \frac{PRT}{16F^2} \frac{1}{J_i} \frac{1}{p_{i,O_2}} \quad (1)$$

where F is the gas constant, T is the temperature, F is the Faraday constant, R is the gas constant and J_i is the inlet gas flow rate per unit area and p_{i,O_2} is the inlet oxygen partial pressure.

Discussion

$p_{O_2} > 10^{-4}$ bar

The impedance spectra were analysed with equivalent circuit modelling to separate and identify the processes contributing. The impedance of a porous mixed ionic and electronic conducting electrode is equivalent to that of a Gerischer element, G, assuming that the AC penetration depth is short compared with the thickness of the electrode [4]

$$Z_{MIEC} = R_e \left(\frac{1}{1 + (\tau_e i\omega)^{n_e}} \right)^{1/2} \quad (2)$$

where R_e represents the electrode polarisation resistance which includes both surface kinetics and solid state transport of oxide ions, $\tau_e = 1/k_e$ is the time constant related to the surface reaction kinetics, which is equal to the inverse of the reaction rate constant, ω is the angular frequency and n_e is an exponent which is included to take into account the depression of the arcs in the Nyquist plot [18]. The impedance spectra obtained were fitted with an equivalent circuit model, $(R_s)(L)(G)$, which consists of a Gerischer element connected in series with a resistor R_s and an inductance, L. The series resistance represents the ohmic loss due to transport of oxide ions in the YSZ electrolyte. The inductance is included to take into account the high-frequency inductance and instrumental artefacts. Figure 10a shows the equivalent model used. For this model, the polarisation resistance, R_p, is equal to the electrode polarisation resistance, R_e.

Figure 11 shows the Nyquist plot for a measurement performed at 0.2 bar and the corresponding model fit. The impedance shown has been normalised by dividing the actual impedance by the polarisation resistance, and the series resistance has been subtracted.

The model then has 5 free parameters where only 3 are related to the oxygen reaction. At 0.2 bar, an inlet

Fig. 10 a The equivalent circuit model $(R_s)(L)(G)$. **b** The equivalent circuit model $(R_s)(L)(G)(R_{mt}Q_{mt})$
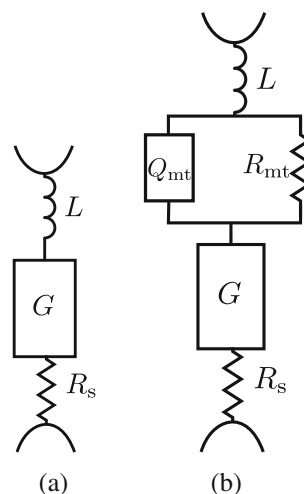
flow rate of 8 L h^{-1} between 600 and 900 °C, n_e was found to be 0.88 ± 0.03. The apparent activation energy of R_e was found to be 1.60 ± 0.03 eV and that of τ_e was found to be 1.80 ± 0.05 eV. The polarisation resistance was found to be proportional to $p_{O_2}^{-0.25}$ at 700 °C. The time constant was found to be proportional to $p_{O_2}^{-0.5}$, and the reaction rate constant was proportional to $p_{O_2}^{0.5}$. A similar dependency of the oxygen partial pressure and the activation energy has previously been observed for other perovskite-type metal oxides [4, 19, 20]. The summit frequency is among others highly dependent on the microstructure of the electrode and the thickness of the electrode [20]. For composite perovskite-type electrodes which have been sintered at similar temperatures with similar electrode thicknesses, the summit frequencies are nearly the same [20, 21].
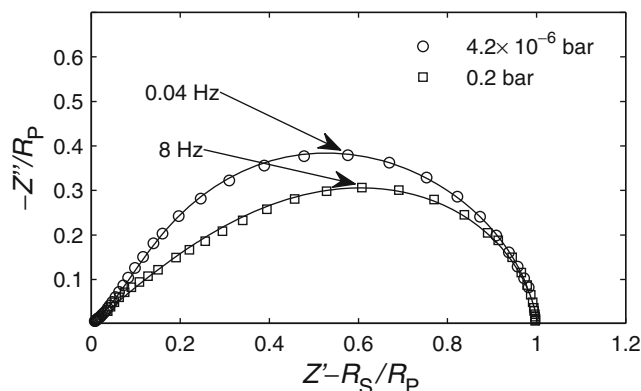

Fig. 11 Nyquist plot of the impedance, normalised with respect to the polarisation resistance, R_p, and corrected for the series resistance, R_s, for measurements performed at 700 °C at oxygen partial pressures of 0.2 and 4.2×10^{-6} bar and at an inlet gas flow rate of 8 L h^{-1}, with fits

$p_{O_2} < 10^{-4}$ bar

The model applied at oxygen partial pressures below 10^{-4} bar has an extra RC circuit, $(R_{mt}C_{mt})$ connected in series, which represents mass transport processes. R_{mt} is the mass transport polarisation resistance and C_{mt} the capacitance related to the mass transport processes [14, 17]. The capacitance, C_{mt}, was replaced by a constant phase element, Q_{mt}, to take into account the depression of the arcs observed [22]. The depression of the arcs was assumed to be similar, $n_{mt} = n_e$, and constrained so that $0.9 < n_e, n_{mt} < 1$ while fitting to decrease the number of free parameters. Furthermore, the constraint $\tau_{mt} > \tau_e$ was applied because the mass transport processes are initiated by the oxygen reaction and thus lagging behind at transient conditions. It is the oxygen reaction which initiates the transport processes. The model, $(R_s)(L)(G)(R_{mt}Q_{mt})$, therefore has 6 free parameters. The model is shown in Fig. 10b, and the fits are shown with solid line in Fig. 11. For this model, the polarisation resistance, R_p, is equal to the sum of the mass transport and the electrode polarisation resistance, $R_e + R_{mt}$. The capacitance of the mass transport processes is given by $C_{mt} = (R_{mt}^{1-n_{mt}}Q_{mt})^{1/n_{mt}}$ [22], where Q_{mt} is a constant phase element and the gas phase mass transport time constant is given by $\tau_{mt} = R_{mt}C_{mt}$.

Figure 8 shows the polarisation resistance as a function of the inverse temperature at an oxygen partial pressure of 10^{-5} bar and an inlet gas flow rate of 8 L h^{-1}. At 900 °C, the polarisation resistances R_{mt} and R_e were found to be 82 and 2.2 Ω cm^2, respectively, and the polarisation resistance increased only slightly with temperature. The polarisation resistance related to gas conversion can be calculated to be $R_C = (PRT/16F^2)(1/J_i)(1/p_{i,O_2}) = 27$ Ω cm^2 where $J_i = 8/0.39$ L h^{-1} cm^{-2} and $p_{i,O_2} = 10^{-5}$ bar [14]. The measured gas conversion resistance is higher because only a part of the inlet gas is converted, probably due to incomplete mixing in the gas space above the working electrode. The polarisation resistance related to the mass transport processes is assumed to be independent of the temperature, and the value of R_{mt}, obtained at 900 °C, was therefore used when fitting the impedance measured at lower temperatures to decrease the number of free parameters.

Below 700 °C, the oxygen reaction kinetics dominated the impedance, and the gas phase mass transport processes were not observed. The Arrhenius plot in Fig. 12 shows that the apparent activation energy of R_e is 1.5 ± 0.2 eV and that of τ_e is 1.0 ± 0.1 eV. It is also seen that between 750 °C and 800 °C, it is difficult to separate the time constants of the mass transport
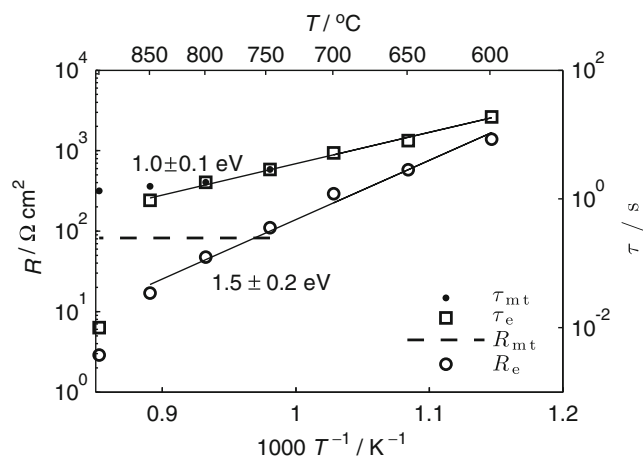

Fig. 12 Arrhenius plot of the time constant and the polarisation resistance at an oxygen partial pressure of 10^{-5} bar and $J_i = 8$ L h^{-1}

processes and the oxygen reaction because the arcs related to these processes overlap in the impedance spectrum. The activation energy of τ_e is decreased compared with the measurements performed at 0.2 bar while that of R_e did not change significantly.

Figure 13 shows the time constant and the polarisation resistance as functions of the oxygen partial pressure. R_{mt} was determined from two measurements performed below an oxygen partial pressures of 10^{-5} bar at 700 °C. Below 10^{-5} bar, the resistance related to the oxygen reaction, R_e, was extrapolated from the measurements performed at higher oxygen partial pressure to be able to determine R_{mt}. It was not difficult to separate the arc related to mass transport processes and that related to the oxygen reaction at 700 °C. Figure 13 indicates that R_{mt} is highly dependent on
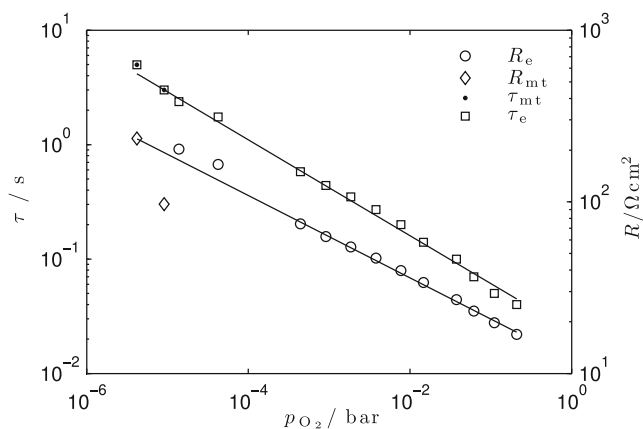

Fig. 13 The time constant and the polarisation resistance as functions of the oxygen partial pressure for measurements performed at 700 °C at an inlet gas flow rate of 8 L h^{-1}

the oxygen partial pressure, as expected for gas phase mass transport processes. Figure 13 shows that it is not possible to separate the time constants related to the oxygen reaction and the gas phase mass transport processes. The graph indicates that the time constant of the mass transport processes increases with decreasing oxygen partial pressure and become dominating at around 10^{-5} bar.

Theoretically, the gas conversion resistance gives rise to a symmetrical semicircle, and the resistance is inversely proportional to the oxygen partial pressure, but the time constant should be independent of the oxygen partial pressure [14]. The size of the capacitance cannot be accounted for using a continuously stirred tank reactor model. The gas conversion time constant is related to the volume of the gas layer as $\tau_C = (J_i RT/P)V_C$ [14], where V_C is the volume of the gas layer. The volume of the gas layer may then be calculated, if the measured mass transport time constant is equal to the gas conversion time constant, to be 29 cm^3, which does not fit with the dimensions of the three-electrode setup. The LSCV stores oxygen by changing stoichiometry and the differential capacitance associated with the change in stoichiometry is given by

$$C = -V_L 2F \frac{dc_V}{dE} \quad (3)$$

where c_V is the concentration of oxide ion vacancies and V_L is the volume of the LSCV $V_L = V_e \phi_L = 15 \times 10^{-4}$ cm $\times 0.39$ cm$^2 \times 1/3 = 1.9 \times 10^{-4}$ cm^3, where $\phi_L = 1/3$ is the volume fraction of LSCV. The vacancy concentration in LSCV is nearly proportional to $p_{O_2}^{-0.5}$ in the oxygen pressure range of the present work, i.e. $c_V = \beta p_{O_2}^{-0.5}$ [23]. Assuming equilibrium is obtained, the potential differentiated with the oxygen partial pressure is given by $dE = (RT/4F)(1/p_{O_2})dp_{O_2}$. The differential capacitance may then be calculated using that

$$-V_L 2F \frac{dc_V}{dE} = -V_L \frac{8F^2}{RT} p_{O_2} \frac{d(\beta p_{O_2}^{-0.5})}{dp_{O_2}} = V_L \frac{4F^2}{RT} c_V \quad (4)$$

where β is some constant. At 700 °C and an oxygen partial pressure of 4.2×10^{-6} bar, the concentration of vacancies was calculated according to Van Hassel et al. [23] at 1,000 °C to be 3.8×10^{-7} mol cm^{-3}, and the calculated capacitance was then 3×10^{-4} F cm^{-2} which is lower compared with the capacitance measured at 700 °C, $C_{mt} = 0.02$ F cm^{-2}. The change in the oxide ion stoichiometry therefore can only account for a part of the capacitance.

Conclusion

A porous composite LSCV/YSZ electrode intended for oxygen sensors was characterised. SEM showed a porous coherent microstructure of the electrode with LSCV and YSZ grain sizes between 200 and 400 nm. The electrochemical properties were characterised by EIS at various oxygen partial pressures, temperatures and inlet gas flow rates. At oxygen partial pressures around 0.2 bar, the oxygen reaction is dominated by solid-state diffusion of oxide ions and surface reaction kinetics. The reaction is distributed through the electrode thereby making it robust and tolerant towards poisoning by impurities. The rate constant related to the oxygen reaction at the LSCV surface is proportional to $p_{O_2}^{0.5}$ and has an activation energy of 1.8 eV.

At oxygen partial pressures around 10^{-5} bar above 800 °C, gas phase mass transport processes dominate the impedance spectra, and the impedance is inversely proportional to the inlet gas flow rate and highly dependent on the oxygen partial pressure. The time constant of the dominating arc and thereby the response time increased with decreasing oxygen partial pressure. LSCV may take up/release oxygen by changing the oxide ion stoichiometry which gives rise to a large capacitance and thereby a slow response time. However, it cannot either account for the size of the capacitance observed. The relatively low response time at 700 °C at an oxygen partial pressure of around 5×10^{-6} bar and an inlet gas flow rate of 8 L h^{-1} makes the robust LSCV/YSZ electrode suitable for use as an industrial oxygen sensor electrode.

References

1. Barbi GB, Casiraghi A, Mari CM (1983) Electrode material for high-temperature oxygen partial pressure electrochemical sensors: strontium-doped lanthanum chromite. Rev Sci Instrum 54(4):486–492
2. Badwal SPS, Ciacchi FT, Haylock JW (1988) Nernstian behaviour of zirconia oxygen sensors incorporating composite electrodes. J Appl Electrochem 18(2):232–239
3. Alcock CB (1992) Perovskite electrodes for sensors. Solid State Ion 51:281–289
4. Adler SB, Lane JA, Steele BCH (1996) Electrode kinetics of porous mixed-conducting oxygen electrodes. J Electrochem Soc 143(11):3554

5. Mitterdorfer A, Gauckler LJ (1999) Identification of the re-
action mechanism of the Pt, O2 (g)| yttria-stabilized zirconia
system part I. Solid State Ion 117(3–4):187–202
6. Mitterdorfer, A, Gauckler LJ (1999) Identification of the re-
action mechanism of the Pt, O2(g)| yttria-stabilized zirconia
system part II. Solid State Ion 117(3–4):203–217
7. Gellings PJ, Bouwmeester HJM (1997) The CRC handbook
of solid state electrochemistry. CRC, New York
8. Shuk P, Bailey E, Guth U (2008) Zirconia oxygen sensor for
the process application: state-of-the-art. Sensors (Peterborough,
NH) 90:174–184
9. Karim DP, Aldred AT (1979) Localized level hopping trans-
port in La (Sr) CrO [sub 3]. Phys Rev B 20(6):2255–2263
10. Fergus J (2004) Lanthanum chromite-based materials for solid
oxide fuel cell interconnects. Solid State Ion 171(1–2): 1–15
11. Larsen PH, Hendriksen PV, Mogensen M (1997) Dimen-
sional stability and defect chemistry of doped lanthanum
chromites. J Therm Anal Calorim 49(3):1263–1275
12. Primdahl S, Hansen JR, Grahl-Madsen L (2001) Sr-doped
LaCrO anode for solid oxide fuel cells. J Electrochem Soc
148(1):74–81
13. Lasia A (2009) Modeling of impedance of porous electrodes.
In: Schlesinger M (ed) Modern aspects of electrochemistry,
vol 43. Springer, Dordrecht, pp 67–137
14. Jacobsen T, Hendriksen P, Koch S (2008) Diffusion and con-
version impedance in solid oxide fuel cells. Electrochim Acta
53(25):7500–7508
15. Chick LA, Pederson LR, Maupin GD, Bates JL, Thomas LE,
Exarhos GJ (1990) Glycine-nitrate combustion synthesis of
oxide ceramic powders. Mater Lett 10(1–2):6–12
16. Badwal SPS (1984) Electrical conductivity of single crys-
tal and polycrystalline yttria-stabilized zirconia. J Mater Sci
19(6):1767–1776
17. Primdahl S, Mogensen M (1998) Gas conversion impedance:
a test geometry effect in characterization of solid oxide fuel
cell anodes. J Electrochem Soc 145(7):2431
18. Boukamp BA, Bouwmeester HJM (2003) Interpretation of
the Gerischer impedance in solid state ionics. Solid State Ion
157(1–4):29–33
19. Adler SB (2004) Factors governing oxygen reduction in solid
oxide fuel cell cathodes. Chem Rev 104(10):4791–843
20. Joergensen MJ, Mogensen M (2001) Impedance of solid ox-
ide fuel cell LSM/YSZ composite cathodes. J Electrochem
Soc 148(5):A433
21. Murray EP, Tsai T, Barnett SA (1998) Oxygen transfer
processes in (La, Sr) MnO3/Y2O3-stabilized ZrO2 cathodes:
an impedance spectroscopy study. Solid State Ion 110(3–
4):235–243
22. Orazem ME, Tribollet B (2008) Electrochemical impedance
spectroscopy. Wiley, Hoboken
23. Van Hassel BA, Kawada T, Sakai N, Yokokawa H, Dokiya
M, Bouwmeester HJM (1993) Oxygen permeation modelling
of perovskites. Solid State Ion 66(3–4):295–305
24. Azegami K, Yoshinaka M, Hirota K, Yamaguchi O (1998)
Formation and sintering of LaCrO3 prepared by the hy-
drazine method. Mater Res Bull 33(2):341–348
25. Mori M, Hiei Y, Sammes NM (1999) Sintering behavior
and mechanism of Sr-doped lanthanum chromites with a
site excess composition in air. Solid State Ion 123(1–4):103–
111